UCRL-ID-139828

A Tow-Level Progressive Damage Model for Simulating Carbon-Fiber Textile Composites: Interim Report

E. Zywicz

July 1, 2000

U.S. Department of Energy
Lawrence Livermore National Laboratory

DISCLAIMER

This work was performed under the auspices of the U. S. Department of Energy by the University of California, Lawrence Livermore National Laboratory under Contract No. W-7405-Eng-48.

A Tow-Level Progressive Damage Model For Simulating Carbon-Fiber Textile Composites: Interim Report

by

Edward Zywicz

University of California
Lawrence Livermore National Laboratory
Structural Mechanics Group

July 1, 2000

Contents

A Tow-Level Progressive Damage Model For Simulating Carbon-Fiber Textile Composites: Interim Report

by

Edward Zywicz

Abstract

A numerical approach to model the elasto-plastic and tensile damage response of tri-axially braided carbon-fiber polymeric-matrix composites is developed. It is micromechanically based and consists of a simplified unit cell geometry, a plane-stress tow-level constitutive relationship, a one-dimensional undulation constitutive law, and a non-traditional shell element integration rule. The braided composite lamina is idealized as periodic in the plane, and a simplified three-layer representative volume (RV) is assembled from axial and braider tows and pure resin regions. The constituents in each layer are homogenized with an iso-strain assumption in the fiber-direction and an iso-stress condition in the other directions. In the upper and lower layers, the fiber-direction strain is additively decomposed into an undulation and a tow portion. A finite-deformation tow model predicts the plane-stress tow response and is coupled to the undulation constitutive relationship. The overall braid model is implemented in DYNA3D and works with traditional shell elements.

The finite-deformation tow constitutive relationship is derived from the fiber elasticity and the isotropic elasto-plastic power-law hardening matrix response using a thermodynamic framework and simple homogenization assumptions. The model replicates tensile damage evolution, in a smeared sense, parallel and perpendicular to the fiber axis and is regularized to yield mesh independent results. The tow-level model demonstrates reasonable agreement, prior to damage, with detailed three-dimensional FE (finite element) elasto-plastic simulations of aligned, periodically arranged, uni-directional composites.

The 3-layer braid model response is compared with predictions obtained from detailed micromechanical simulations of the braid's unit cell in uni-axial extension, shear, and flexure for three braid angles. The elastic properties show good agreement as does the non-linear response for loadings dominated by the axial tows. In loadings dominated by the braider tow response, the absence of a non-linear undulation model deteriorates the agreement. Nonetheless, the present approach is applicable to a broad range of tri-axially braided composites as well as for uni-directional composites, but presently lacks any compressive failure mechanisms and an adequate non-linear undulation model.

1 Introduction

Large-tow carbon-fiber textile composites contain many unique features that must be addressed when modeling their behavior. The elastic properties of textile composites have been calculated using a variety of numerical and micromechanical techniques as summarized in Naik (1995) and Carrier and Averill (2000). Naik (1995) developed an idealized three-dimensional (3-D) representative unit cell (RUC) geometry. He subdivided the RUC, expressed the local stiffness each sub-cell in the global coordinate system, and applied iso-strain assumptions to calculate the effective extensional RUC elastic properties. To capture the bending and straightening/wrinkling undulation behavior, an undulation model was derived from the solution for an elastic beam on an elastic foundation and used in the undulation slice region. The predicted elastic braid properties showed good agreement with experimental values.

Carrier and Averill (2000) used Naik's RUC geometry and constructed a finite element (FE) unit cell with beam and shell elements. The former element type represented the fiber tows and the later the surplus resin. They adapted Naik's undulation model to calculate a fiber-direction reduction factor and applied it to the fiber-direction modulus in the braider tows to account for the undulation. Their effective elastic properties agreed favorably with those of Naik.

Zywicz and Nguyen (1999) developed a detailed FE model with hexahedral elements based on Naik's RUC and explored the extensional and flexural response of large-tow carbon-fiber tri-axial braids. Like Whitcomb *et al* (1998), they placed element faces coincidental with tow-resin and tow-tow interfaces, and found that the effective lamina extensional and flexural elastic properties are distant quantities, not derivable from one another. This was attributed to their large microstructural size and non-homogeneous fiber distribution. Zywicz *et al* (2000) extended this theoretical work to address other braid angles as well as to predict their elasto-plastic response under uni-axial extension, shear, and flexure.

The non-linear behavior has been investigated as well. Naik (2000) incorporated an incremental non-linear shear response and a stiffness reduction-based orthotropic damage model to predict the RUC response and overall strength. The in-plane shear stress-strain response was given by a three term expression. Four tow-level failure criterion were used. When a criteria was satisfied, select moduli in the sub-cell were reduced by 80% to 99%. The model predictions agreed well with their experimental results.

Unfortunately, the detailed non-linear approaches used by Naik (1995) and Zywicz *et al* (2000) are not useful in large-scale numerical calculations due to their computational expense. Furthermore, the treatment of damage in Naik's work contains no inherent length scale or energy quantity and may be overly conservative in some applications. The later can cause incorrect subsequent or collateral damage modes to be initiated.

The present work develops a simple micromechanically based numerical technique to represent carbon-fiber textile composites in large-scale vehicular crashworthiness simulations. First, a tow-level elasto-plastic constitutive law with tensile damage is developed from the basic fiber and matrix properties and behaviors. The individual constituent behaviors are homogenized using a geometry independent approach, and the damage portion of the constitutive law is regularized to yield mesh independent results. The elasto-plastic tow response is compared with results from detailed 3-D micromechanical models. Next, a simplified braid geometry is constructed from Naik's RUC and is explicitly defined in terms of its local microstructural features. Following that, a 3-layer numerical model is assembled. The resin region and tow constitutive behavior in each layer are homogenized. An explicit undulation model is outlined and coupled to the tow model by additively decomposing the fiber-direction strain and enforcing an approximate one-dimensional iso-stress assumption. The through-thickness integration requirements necessary to implement the 3-layer model in traditional shell elements are presented. In the next section, the numerical 3-layer braid model is validated by comparing results from it and detailed elasto-plastic 3-D FE simulations of several tri-axial braids. Lastly, a short summary of the model is presented and missing features are identified.

2 Tow-Level Constitutive Model

A plane-stress constitutive model is derived for a continuous, uni-directional, fiber composite tow. The tow is assumed to be made up of many fiber-level RVEs. Each RVE contains a single fiber and its adjacent matrix material. Within the RVE, a local material coordinate system is constructed such that the 1-axis parallels the local axial fiber direction and the 3-axis points out of the lamina plane. The fiber is idealized as a transversely isotropic elastic solid and the matrix is taken as an isotropic elasto-plastic solid with J2 power-law hardening.

The tow model is presented in three sections. The first section describes the homogenization process used to construct the effective composite response from the individual

fiber and matrix responses. The second section presents the plane-stress plasticity relations, and the last section discusses the tensile damage mechanisms.

2.1 Tow-Level Homogenization

The basic constitutive relationships, which are used to relate the average RVE stress to the average RVE strain in each constituent, are given by

$$\boldsymbol{\sigma}^f = \boldsymbol{C}^f : \boldsymbol{\epsilon}^f \qquad \text{and} \qquad \boldsymbol{\sigma}^m = \boldsymbol{C}^m : (\boldsymbol{\epsilon}^m - \boldsymbol{\epsilon}^{mp}), \tag{1}$$

where

$$\boldsymbol{S} = \boldsymbol{C}^{-1} = \begin{bmatrix} S_{11} & S_{12} & 0 & 0 & 0 \\ S_{12} & S_{22} & 0 & 0 & 0 \\ 0 & 0 & S_{44} & 0 & 0 \\ 0 & 0 & 0 & S_{55} & 0 \\ 0 & 0 & 0 & 0 & S_{66} \end{bmatrix}, \tag{2}$$

$\boldsymbol{\sigma} = \{\sigma_{11}, \sigma_{22}, \sigma_{12}, \sigma_{23}, \sigma_{13}\}^T$, $\boldsymbol{\epsilon} = \{\epsilon_{11}, \epsilon_{22}, 2\epsilon_{12}, 2\epsilon_{13}, 2\epsilon_{23}\}^T$, and the superscripts f, m, c, and p denote fiber, matrix, composite, and plastic quantities, respectively. (Bold quantities denote vectors and matrices, and bold calligraphic variables represent 4-th order tensors. The operator ":" implies an inner product. The superscripts T and -1 define the matrix transpose and inverse operations, respectively.) The initial components of the compliance tensor $\boldsymbol{S}$ are defined in the traditional manner, *e.g.*, see Jones (1975).

The RVE is homogenized by enforcing an iso-strain condition in the fiber direction and iso-stress conditions in the other directions, *i.e.*,

$$\epsilon_{11}^c = \epsilon_{11}^f = \epsilon_{11}^m \tag{3}$$

and

$$\sigma_i^c = \sigma_i^f = \sigma_i^m \qquad i = 2, 3, 4, 5. \tag{4}$$

The remaining composite stress and strain terms are given by

$$\sigma_{11}^c = v^m \sigma_{11}^m + v^f \sigma_{11}^f \tag{5}$$

and

$$\epsilon_i^c = v^m \epsilon_i^m + v^f \epsilon_i^f \qquad i = 2, 3, 4, 5, \tag{6}$$

where v^f and v^m are the fiber and matrix volume fractions.

With the present homogenization and constituent assumptions, it is possible to develop a simple, compact form, for the RVE constitutive relationship. For convenience, define the reduced stress and strain vectors, $\boldsymbol{\tau}$ and $\boldsymbol{\gamma}$, respectively, as $\boldsymbol{\tau} = \{\sigma_{22}, \sigma_{12}, \sigma_{23}, \sigma_{13}\}^T$ and $\boldsymbol{\gamma} = \{\epsilon_{22}, 2\epsilon_{12}, 2\epsilon_{23}, 2\epsilon_{13}\}^T$. From (1) and (2), the reduced fiber relationship is expressible as

$$\boldsymbol{\tau} = C_{12}^f \, \epsilon_{11}^c \, \boldsymbol{p} + \bar{\boldsymbol{C}}^f : \boldsymbol{\gamma}^f \tag{7}$$

where

$$\bar{C}_{ij}^f = C_{i+1,j+1}^f \qquad i,j = 1,2,3,4 \tag{8}$$

and $\boldsymbol{p} = \{1,0,0,0\}^T$. Solving (7) for $\boldsymbol{\gamma}^f$ yields

$$\boldsymbol{\gamma}^f = \bar{\boldsymbol{C}}^{f\,-1} : \left\{\boldsymbol{\tau}^f - C_{12}^f \, \epsilon_{11}^c \, \boldsymbol{p}\right\}, \tag{9}$$

which, when substituted into (6) and rearranged, gives the reduced matrix strain vector as

$$\boldsymbol{\gamma}^m = \left\{\boldsymbol{\gamma}^c - v^f \bar{\boldsymbol{C}}^{f\,-1} : \left\{\boldsymbol{\tau}^f - C_{12}^f \, \epsilon_{11}^c \, \boldsymbol{p}\right\}\right\} \frac{1}{v^m}. \tag{10}$$

Inserting (10) into the matrix law (1) gives

$$\boldsymbol{\sigma}^m = \boldsymbol{C}^m : \left\{ \left\{ \begin{array}{c} \epsilon_{11}^c \\ \left(\boldsymbol{\gamma}^c + C_{12}^f \, \epsilon_{11}^c \, \boldsymbol{p}\right)/v^m \end{array} \right\} - \boldsymbol{\epsilon}^{mp} \right\} - \boldsymbol{C}^m : \left\{ \begin{array}{c} 0 \\ v^f \bar{\boldsymbol{C}}^{f\,-1} : \boldsymbol{\tau}^f \end{array} \right\} \frac{1}{v^m} \tag{11}$$

and by noting that $\boldsymbol{\tau}^f = \boldsymbol{\tau}^m = \boldsymbol{\tau}^c$, it can be alternatively written as

$$\boldsymbol{\sigma}^m + \frac{v^f}{v^m} \boldsymbol{C}^m : \left\{ \begin{array}{c} 0 \\ \bar{\boldsymbol{C}}^{f\,-1} : \boldsymbol{\tau}^c \end{array} \right\} = \boldsymbol{C}^m : \left\{ \left\{ \begin{array}{c} \epsilon_{11}^c \\ \left(\boldsymbol{\gamma}^c + C_{12}^f \, \epsilon_{11}^c \, \boldsymbol{p}\right)/v^m \end{array} \right\} - \boldsymbol{\epsilon}^{mp} \right\}. \tag{12}$$

To simplify (12), define $\tilde{\boldsymbol{S}}^f$ as

$$\tilde{\boldsymbol{S}}^f = \begin{bmatrix} 0 & 0 & 0 & 0 & 0 \\ 0 & \bar{C}_{11}^{f\,-1} & \bar{C}_{12}^{f\,-1} & \bar{C}_{13}^{f\,-1} & \bar{C}_{14}^{f\,-1} \\ 0 & \bar{C}_{21}^{f\,-1} & \bar{C}_{22}^{f\,-1} & \bar{C}_{23}^{f\,-1} & \bar{C}_{24}^{f\,-1} \\ 0 & \bar{C}_{31}^{f\,-1} & \bar{C}_{32}^{f\,-1} & \bar{C}_{33}^{f\,-1} & \bar{C}_{34}^{f\,-1} \\ 0 & \bar{C}_{41}^{f\,-1} & \bar{C}_{42}^{f\,-1} & \bar{C}_{43}^{f\,-1} & \bar{C}_{44}^{f\,-1} \end{bmatrix} \tag{13}$$

and the effective matrix strain, $\boldsymbol{\epsilon}^{\bar{e}}$, as

$$\boldsymbol{\epsilon}^{\bar{e}} = \boldsymbol{B} : \boldsymbol{\epsilon}^c = \left\{ \begin{array}{c} \epsilon_{11}^c \\ \left(\boldsymbol{\gamma}^c + v^f q \, \epsilon_{11}^c \, \boldsymbol{p}\right) \frac{1}{v^m} \end{array} \right\}, \tag{14}$$

where

$$\boldsymbol{B} = \begin{bmatrix} 1 & 0 & 0 & 0 & 0 \\ q\,v^f/v^m & 1/v^m & 0 & 0 & 0 \\ 0 & 0 & 1/v^m & 0 & 0 \\ 0 & 0 & 0 & 1/v^m & 0 \\ 0 & 0 & 0 & 0 & 1/v^m \end{bmatrix} \tag{15}$$

and, assuming $\boldsymbol{C}^f$ possesses transverse isotropy,

$$q = -S^f_{12}/S^f_{11}. \tag{16}$$

Consequently, (12) can be written and solved for $\boldsymbol{\sigma}^m$ to give

$$\boldsymbol{\sigma}^m = \boldsymbol{\mathcal{D}} : \{\boldsymbol{\epsilon}^{\bar{e}} - \boldsymbol{\epsilon}^{mp}\}, \tag{17}$$

where

$$\boldsymbol{\mathcal{D}} = \left(\boldsymbol{I} + \frac{v^f}{v^m}\boldsymbol{C}^m\tilde{\boldsymbol{S}}\right)^{-1}\boldsymbol{C}^m, \tag{18}$$

$\boldsymbol{I}$ is the 5×5 identity matrix, and $\boldsymbol{\mathcal{J}} = \boldsymbol{\mathcal{D}}^{-1}$.

Aside: with the assistance of a symbolic mathematical manipulator, the non-zero components of $\boldsymbol{\mathcal{J}}$, expressed in matrix form, can be shown to be:

$$J_{11} = S^m_{11} \tag{19}$$

$$J_{12} = S^m_{12} \tag{20}$$

$$J_{22} = S^m_{22} + \frac{v^f}{v^m}\left(S^f_{22} - S^{f\,2}_{12}/S^f_{11}\right) \tag{21}$$

$$J_{33} = S^m_{44} + \frac{v^f}{v^m}S^f_{44} \tag{22}$$

$$J_{44} = S^m_{44} + \frac{v^f}{v^m}S^f_{55} \tag{23}$$

$$J_{55} = S^m_{44} + \frac{v^f}{v^m}S^f_{44} \tag{24}$$

The fiber stress can now be expressed in a similar form. From (1) and (2), the fiber axial stress is given by

$$\sigma^f_{11} = \frac{e^c_{11}}{S^f_{11}} - \frac{S^f_{12}}{S^f_{11}}\sigma^c_{22}. \tag{25}$$

With $\boldsymbol{E}$ and $\boldsymbol{H}$ defined as

$$\boldsymbol{E} = \begin{bmatrix} v^f/S^f_{11} & 0 & 0 & 0 & 0 \\ 0 & 0 & 0 & 0 & 0 \\ 0 & 0 & 0 & 0 & 0 \\ 0 & 0 & 0 & 0 & 0 \\ 0 & 0 & 0 & 0 & 0 \end{bmatrix} \quad \text{and} \quad \boldsymbol{H} = \begin{bmatrix} 0 & q & 0 & 0 & 0 \\ 0 & 1 & 0 & 0 & 0 \\ 0 & 0 & 1 & 0 & 0 \\ 0 & 0 & 0 & 1 & 0 \\ 0 & 0 & 0 & 0 & 1 \end{bmatrix}, \tag{26}$$

$\boldsymbol{\sigma}^f$ is alternatively given by

$$\boldsymbol{\sigma}^f = \frac{1}{v^f}\boldsymbol{E} : \boldsymbol{\epsilon}^c + \boldsymbol{H} : \boldsymbol{\sigma}^m \tag{27}$$

$$= \frac{1}{v^f}\boldsymbol{E} : \boldsymbol{\epsilon}^c + \boldsymbol{H}\boldsymbol{\mathcal{D}} : \{\boldsymbol{\epsilon}^{\bar{e}} - \boldsymbol{\epsilon}^{mp}\}. \tag{28}$$

With the fiber and matrix stresses expressed in similar forms, the composite stress can now be assembled. Because $v^m + v^f = 1$, equations (4) and (5) can be combined and written as

$$\boldsymbol{\sigma}^c = v^m\boldsymbol{\sigma}^m + v^f\boldsymbol{\sigma}^f. \tag{29}$$

Substitution of (17) and (28) into the previous expression yields

$$\boldsymbol{\sigma}^c = \begin{Bmatrix} \left(\left(\epsilon^c_{11}/S^f_{11}\right) + q\sigma^m_{22}\right)v^f \\ 0 \\ 0 \\ 0 \\ 0 \end{Bmatrix} + \begin{Bmatrix} v^m\sigma^m_{11} \\ \sigma^m_{22} \\ \sigma^m_{12} \\ \sigma^m_{23} \\ \sigma^m_{13} \end{Bmatrix} \tag{30}$$

$$= \boldsymbol{E} : \boldsymbol{\epsilon}^c + \left(v^f\boldsymbol{H} + v^m\boldsymbol{I}\right)\boldsymbol{\mathcal{D}} : \{\boldsymbol{\epsilon}^{\bar{e}} - \boldsymbol{\epsilon}^{mp}\} \tag{31}$$

$$= \boldsymbol{E} : \boldsymbol{\epsilon}^c + \boldsymbol{G}\boldsymbol{\mathcal{D}} : \{\boldsymbol{\epsilon}^{\bar{e}} - \boldsymbol{\epsilon}^{mp}\}, \tag{32}$$

where

$$\boldsymbol{G} = \begin{bmatrix} v^m & v^f q & 0 & 0 & 0 \\ 0 & 1 & 0 & 0 & 0 \\ 0 & 0 & 1 & 0 & 0 \\ 0 & 0 & 0 & 1 & 0 \\ 0 & 0 & 0 & 0 & 1 \end{bmatrix}. \tag{33}$$

In the absence of matrix plasticity, *i.e.* $\boldsymbol{\epsilon}^{mp} = \mathbf{0}$, (32) reduces to

$$\boldsymbol{\sigma}^c = (\boldsymbol{E} + \boldsymbol{G}\boldsymbol{\mathcal{D}}\boldsymbol{B}) : \boldsymbol{\epsilon}^c \tag{34}$$

and the parenthetical quantity is the effective composite stiffness.

The effective composite elastic properties are transversely isotropic and are given by:

$$E^c_{11} = v^f E^f_{11} + v^m E^m \tag{35}$$

$$E^c_{22} = \frac{E^f_{11}E^f_{22}E^mE^c_{11}}{E^c_{11}E^f_{11}\left(v^fE^m + v^mE^f_{22}\right) - E^f_{22}v^fv^m\left(E^m\nu^f_{12} - E^f_{11}\nu^m\right)^2} \tag{36}$$

$$\mu^c_{12} = \frac{\mu^m\mu^f_{12}}{\mu^f_{12}v^m + \mu^m v^f} \tag{37}$$

$$\mu_{12}^{c*} = \frac{1}{2}\left(\mu_{12}^{c} + \frac{\mu^m\left(\mu^m v^m + \mu_{12}^f\left(1+v^f\right)\right)}{\mu^m\left(1+v^f\right)\mu_{12}^f v^m}\right) \tag{38}$$

$$\mu_{23}^{c} = \frac{\mu^m \mu_{23}^f}{\mu_{23}^f v^m + \mu^m v^f} \tag{39}$$

$$\nu_{12}^{c} = v^f \nu_{12}^f + v^m \nu^m \tag{40}$$

$$\nu_{23}^{c} = \frac{E_{22}^{c}}{2\mu_{23}^{c}} - 1 \tag{41}$$

Unfortunately, as described in the subsequent validation section, μ_{12}^c underestimates the value obtained when the fibers are assumed to be in either cylindrical, square, or hexagonal packing arrays. Thus, the Hasin and Rosen (1964) cylinder estimate, as presented in Hashin (1983), is averaged with the present estimate to yield μ_{12}^{c*}, the value employed in this model. Note, this requires that $\mathcal{J}_{33}$ be redefined as $\mathcal{J}_{33} = 1/(v^m\,\mu_{12}^{c*})$.

In application, equations (17), (25), and (30) provide a more efficient way to determine the tow stress than (32). This is because (17) is identical in form to the original matrix constitutive relationship. Consequently, the plasticity rules governing the underlying matrix relationship apply directly to the pseudo-matrix response represented by (17).

2.2 Finite Deformation

Orthotropic damage models that use stiffness enhancement (as used here) or compliance degradation to represent smeared damage and are formulated with a traditional hypoelastic framework can demonstrate undesirable behavior in FE implementations. For example, assume that the constitutive model is given by

$$\boldsymbol{\sigma}^{\nabla} = \boldsymbol{C}\left(\boldsymbol{d}\right) : \left\{\dot{\boldsymbol{\epsilon}} - \dot{\boldsymbol{\epsilon}}^p\right\}, \tag{42}$$

where $\boldsymbol{\sigma}^{\nabla}$ is the Jaumann stress rate, $\boldsymbol{d}$ is a vector of internal variables, and $\dot{\boldsymbol{\epsilon}}$ is the symmetric part of the velocity gradient $\boldsymbol{L}$. Consider a single cubic hexahedral element whose sides are of unit dimension and are aligned with a Cartesian coordinate system. Assume that all Poisson's ratios are zero, although not necessary, and that at the strain state $\boldsymbol{\epsilon}^* =< \epsilon_{11}^*, \epsilon_{22}^*, 0, 0, 0, 0 >^t$, the material is fully damaged in the 1-direction and virgin in the other directions. The net force acting on the element side whose normal points in the positive 2-direction is given by

$$f_2 \approx \left(1 + \epsilon_{11}^*\right) C_{22}\, \epsilon_{22}^* \tag{43}$$

Now, stretch the element so that only the strain in the 1-direction increases. From (43), the normal force acting in the direction transverse to the straining direction increases even though ϵ_{22} remains fixed. While the transverse stiffening is small when $\epsilon_{11} \ll 1$, in actual application there is no guarantee that this will be true. In order to eliminate this artificial stiffening, $\boldsymbol{C}$ must depend upon the deformation or some additional mechanism must be used. Such problems are common with damage models, *e.g.,* see Bažant and Planas (1998).

An alternative method that eliminates artificial transverse stiffening is to develop the constitutive relationship with the second Piola-Kirchhoff stress, $\tilde{\boldsymbol{T}}$, and an appropriate strain measure. When $\tilde{\boldsymbol{T}}$ is transformed to the Cauchy stress to perform element integration, the stress is scaled by the deformation such that the net element force remains essentially unchanged. (For additional details, see Malvern, 1969.) The disadvantage of using $\tilde{\boldsymbol{T}}$ occurs in picking a strain measure and constructing damage surfaces since directional orthogonality is not preserved with deformation.

The apparent natural choice for strain is to use the Green-St. Venant strain, $\boldsymbol{E}$, which is the work conjugate measure to $\tilde{\boldsymbol{T}}$. Unfortunately, the physical interpretation of $\boldsymbol{E}$ degenerates when shear strains of 10% or more accumulate. Specifically, the volumetric portion of $\boldsymbol{E}$ is influenced by the shears and vice versa (Bažant and Planas, 1998). Also, the normal strains are "quadratic" functions of the stretches. An alternative strain measure that is linear in stretch is the "U-based" strain, $\boldsymbol{e}$, defined as

$$\boldsymbol{e} = \boldsymbol{U} - \boldsymbol{I} \tag{44}$$

where $\boldsymbol{U}$ is the right stretch tensor and $\boldsymbol{I}$ is the identify matrix.

The constitutive model is implemented using the finite deformation measures $\tilde{\boldsymbol{T}}$ and $\boldsymbol{e}$. However, for presentation purposes, the stress and strain vectors are denoted by $\boldsymbol{\sigma}$ and $\boldsymbol{\epsilon}$ in this manuscript. In order to use $\tilde{\boldsymbol{T}}$ and $\boldsymbol{e}$, it is necessary to calculate the deformation gradient $\boldsymbol{F}$. In shell elements, direct determination of $\boldsymbol{F}$ is not possible since the through-thickness displacement is not known *a priori.* A procedure has been employed by Puso and Weiss (1997) that skirts this problem and is based upon a recursive formula for the determination of $\boldsymbol{F}$. The formula is given by

$$\boldsymbol{F}_{t+\Delta t} = \boldsymbol{F}_t + \Delta t\, \boldsymbol{L}_{t+\Delta t/2} \boldsymbol{F}_t, \tag{45}$$

where Δt is the time increment. At the beginning of the time step, trial values of $\boldsymbol{L}_{t+\Delta t/2}$ and $\boldsymbol{F}_{t+\Delta t}$ are formed assuming the through-thickness velocity component is

zero. The constitutive equation and through-thickness strain are updated based on the approximated value of $\boldsymbol{F}_{t+\Delta t}$. The resulting through-thickness strain increment is then used to infer the unknown velocity allowing $\boldsymbol{L}_{t+\Delta t/2}$ and $\boldsymbol{F}_{t+\Delta t}$ to be properly updated.

2.3 Tensile Damage

Orthotropic tensile damage mechanisms are incorporated into the individual fiber and matrix constitutive relationships and are derived using a general thermodynamic framework, *e.g.*, see Govindjee, Kay, and Simo (1995), Hansen and Schreyer (1994), and Zywicz (1997). Compliance enhancement is used to represent the smeared effect that crack nucleation and growth has on the material. Two crack directions are depicted in the present work. A smeared crack whose normal parallels the 1-axis replicates the behavior of cracks in the matrix and fiber associated with fiber breakage and is included in both the fiber and matrix models. A second smeared crack, parallel to the 2-axis, simulates matrix splitting and/or fiber-matrix interface debonding and is included only in the matrix model.

The damage constitutive relationship is derived first for a generic elasto-plastic material with arbitrary elastic symmetry. The derivation clearly shows that the plasticity relationship, described in the next section, is fully compatible with the present generic formulation. The derivation directly yields the matrix model and, after elimination of the plasticity and second damage mechanism, the fiber model. For practical and numerical reasons, several simplifying assumptions are made that allow the separate fiber and matrix stress-based fiber-damage models to be replaced by a combined, nearly equivalent, strain-based relationship.

2.3.1 Generic Constitutive Formulation

A free energy function is postulated with the form

$$\Psi = (\boldsymbol{\epsilon} - \boldsymbol{\epsilon}^p) : \boldsymbol{C}(\boldsymbol{d}) : (\boldsymbol{\epsilon} - \boldsymbol{\epsilon}^p) + \Psi_d(\boldsymbol{d}) + \Psi_p(\bar{\epsilon}^p), \tag{46}$$

where $\boldsymbol{d}$ is the vector of damage variables, and Ψ_p and Ψ_d are the plastic and damage potentials (defined later). Enforcement of the 2nd law of thermodynamics necessitates that energy dissipation be non-negative and requires that

$$-\dot{\Psi} + \boldsymbol{\sigma} : \dot{\boldsymbol{\epsilon}} \geq 0, \tag{47}$$

or, alternatively, as

$$\dot{\boldsymbol{\epsilon}} : (\boldsymbol{\sigma} - \boldsymbol{C}(\mathbf{d}) : \boldsymbol{\epsilon}^e) - \frac{1}{2}\boldsymbol{\epsilon}^e : \dot{\boldsymbol{C}}(\mathbf{d}) : \boldsymbol{\epsilon}^e + \dot{\mathbf{d}} : \frac{\partial \Psi_d}{\partial \mathbf{d}} - \dot{\boldsymbol{\epsilon}}^p : \boldsymbol{C}(\mathbf{d}) : \boldsymbol{\epsilon}^e + \dot{\bar{\epsilon}}^p : \frac{\partial \Psi_p}{\partial \bar{\epsilon}^p} \geq 0. \tag{48}$$

This inequality must hold true for arbitrary values of $\dot{d}$, $\dot{\epsilon}$, and $\dot{\epsilon}^p$. Following Simo (1989), the constitutive law is taken as

$$\sigma = \mathcal{C}(\mathbf{d}) : \epsilon^e, \tag{49}$$

and the damage and plastic dissipations are individually required to be non-negative, *i.e.*,

$$D_d = -\frac{1}{2}\epsilon^e : \dot{\mathcal{C}}(\mathbf{d}) : \epsilon^e + \dot{\mathbf{d}} : \frac{\partial \Psi_d}{\partial \mathbf{d}} \geq 0 \tag{50}$$

$$D_p = -\dot{\epsilon}^p : \mathcal{C}(\mathbf{d}) : \epsilon^e + \dot{\bar{\epsilon}}^p : \frac{\partial \Psi_p}{\partial \bar{\epsilon}^p} \geq 0. \tag{51}$$

The damage surfaces are defined as

$$\phi_{di} = \sqrt{\sigma : \mathcal{M}_i : \sigma} - \sigma_{fi}\left[(1-\delta)\exp\left(-d_i/d_{oi}\right) + \delta\right], \tag{52}$$

where σ_f is the tensile failure strength, d_o is a material property, δ is a retention factor, and $i = 1, 2$ denote the damage expressions for the fiber-direction damage and transverse damage mechanisms, respectively. The crack-plane tensors, $\mathcal{M}_i$, are given by, in compact notation,

$$\mathcal{M}_1 = \begin{bmatrix} <\sigma_{11}> & 0 & 0 & 0 & 0 \\ 0 & 0 & 0 & 0 & 0 \\ 0 & 0 & (\sigma_{12f}/\sigma_{f1})^2 & 0 & 0 \\ 0 & 0 & 0 & 0 & 0 \\ 0 & 0 & 0 & 0 & (\sigma_{13f}/\sigma_{f1})^2 \end{bmatrix} \tag{53}$$

and

$$\mathcal{M}_2 = \begin{bmatrix} 0 & 0 & 0 & 0 & 0 \\ 0 & <\sigma_{22}> & 0 & 0 & 0 \\ 0 & 0 & (\sigma_{12f}/\sigma_{f2})^2 & 0 & 0 \\ 0 & 0 & 0 & (\sigma_{23f}/\sigma_{f2})^2 & 0 \\ 0 & 0 & 0 & 0 & 0 \end{bmatrix}. \tag{54}$$

The quantities σ_{12f}, σ_{23f} and σ_{13f} are the shear failure strengths, and $<*>$ is 1 when $* \geq 0$, and zero otherwise. Define the damage potential Ψ_d as

$$\Psi_d = \sum_{i=1}^{2} \sigma_{fi}\left(d_{oi}\exp\left(\frac{-d_i}{d_{oi}}\right) + d_i\right), \tag{55}$$

and the work conjugate variable to d_i and $\bar{\epsilon}^p$ as

$$r_{di} = \frac{-\partial \Psi_d}{\partial d_i} = \sigma_{fi}\left(1 - \exp\left(\frac{-d_i}{d_{oi}}\right)\right) \tag{56}$$

and

$$r^p = \frac{-\partial \Psi_p}{\partial \bar{\epsilon}^p}. \tag{57}$$

Adopting the definition in (49), (50) and (51) are satisfied only when

$$-\frac{1}{2}\boldsymbol{\epsilon} : \dot{\boldsymbol{\mathcal{C}}} : \boldsymbol{\epsilon} + \boldsymbol{r}_d : \boldsymbol{d} \geq 0 \tag{58}$$

and

$$-\dot{\epsilon}^p : \boldsymbol{\mathcal{C}} : \boldsymbol{\epsilon}^e + r^p \, \dot{\bar{\epsilon}}^p \geq 0. \tag{59}$$

The evolution equations are obtained by individually maximizing the energy dissipation for plasticity and damage. Define the modified dissipation equations as

$$L_p\left(\boldsymbol{\sigma}, r^p, \lambda_p\right) \equiv -\dot{\epsilon}^p : \boldsymbol{\sigma} - \dot{\bar{\epsilon}}^p \, q^p + \lambda_p \phi_p \tag{60}$$

$$L_d\left(\boldsymbol{\sigma}, \boldsymbol{r}_d, \boldsymbol{\lambda}_d\right) \equiv \frac{1}{2}\dot{\boldsymbol{\sigma}} : \dot{\boldsymbol{\mathcal{S}}} : \boldsymbol{\sigma} + q_1 \dot{d}_1 + q_2 \dot{d}_2 - \lambda_{d1}\phi_{d1} - \lambda_{d2}\phi_{d2}, \tag{61}$$

noting that $\boldsymbol{\epsilon} : \dot{\boldsymbol{\mathcal{C}}} : \boldsymbol{\epsilon} = -\boldsymbol{\sigma} : \dot{\boldsymbol{\mathcal{S}}} : \boldsymbol{\sigma}$ and λ are Lagrange multipliers. Maximization of L_p and L_d requires that

$$\frac{\partial L_p}{\partial \boldsymbol{\sigma}} = \frac{\partial L_p}{\partial \lambda_p} = \frac{\partial L_p}{\partial q^p} = 0$$

and

$$\frac{\partial L_d}{\partial \boldsymbol{\sigma}} = \frac{\partial L_d}{\partial \lambda_{d1}} = \frac{\partial L_d}{\partial \lambda_{d2}} = \frac{\partial L_d}{\partial r_{d1}} = \frac{\partial L_d}{\partial r_{d2}} = 0,$$

respectively. Enforcement of these conditions implies that for the plasticity relationships

$$\frac{\partial L_p}{\partial \boldsymbol{\sigma}} = 0 \;\Rightarrow\; \dot{\epsilon}^p = \lambda_p \frac{\partial \phi_p}{\partial \boldsymbol{\sigma}} \tag{62}$$

$$\frac{\partial L_p}{\partial \lambda_p} = 0 \;\Rightarrow\; \phi_p = 0 \quad \text{when} \quad \lambda_p \neq 0 \tag{63}$$

$$\frac{\partial L_p}{\partial q^p} = 0 \;\Rightarrow\; \dot{\bar{\epsilon}}^p = \lambda_p \frac{\partial \phi_p}{\partial r^p}, \tag{64}$$

and for the damage relationships

$$\frac{\partial L_d}{\partial \boldsymbol{\sigma}} = 0 \;\Rightarrow\; \dot{\boldsymbol{\mathcal{S}}} : \boldsymbol{\sigma} = \lambda_{d1}\frac{\partial \phi_{d1}}{\partial \boldsymbol{\sigma}} + \lambda_{d2}\frac{\partial \phi_{d2}}{\partial \boldsymbol{\sigma}} \tag{65}$$

$$\frac{\partial L_d}{\partial \lambda_{d1}} = 0 \;\Rightarrow\; \phi_{d1} = 0 \quad \text{when} \quad \lambda_{d1} \neq 0 \tag{66}$$

$$\frac{\partial L_d}{\partial \lambda_{d2}} = 0 \;\Rightarrow\; \phi_{d2} = 0 \quad \text{when} \quad \lambda_{d2} \neq 0 \tag{67}$$

$$\frac{\partial L_d}{\partial r_{d1}} = 0 \;\Rightarrow\; \lambda_{d1} = \dot{d}_1 \tag{68}$$

$$\frac{\partial L_d}{\partial r_{d2}} = 0 \;\Rightarrow\; \lambda_{d2} = \dot{d}_2. \tag{69}$$

The plasticity relationship defined by (62)-(64) is equivalent to the one defined for the matrix by equations (92)-(95) in the next section since λ and λ_p are proportional. Note too, that in the proposed form, the plasticity and damage evolutions equations are independent.

The damage evolution equations can be explicitly calculated. Substitution of (68) and (69) into (65) and noting that $\phi_{di} = 0$ when $\dot{d}_i \neq 0$ yields

$$\dot{\boldsymbol{\mathcal{S}}} : \boldsymbol{\sigma} = \sum_{i=1}^{2} \dot{d}_i \frac{\boldsymbol{\mathcal{M}}_i : \boldsymbol{\sigma}}{\sigma_{fi} \left((1-\delta) \exp\left(-d_i/d_{oi}\right) + \delta \right)}. \tag{70}$$

Since $\boldsymbol{\mathcal{M}}_i$ is, in general, singular, the solution of (70) is non-unique. Nonetheless, it is *assumed* that (70) can be expressed as

$$\dot{\boldsymbol{\mathcal{S}}} = \sum_{i=1}^{2} \dot{d}_i \frac{\boldsymbol{\mathcal{M}}_i}{\sigma_{fi} \left((1-\delta) \exp\left(-d_i/d_{oi}\right) + \delta \right)}. \tag{71}$$

which after integrations yields

$$\boldsymbol{\mathcal{S}}(d) = \boldsymbol{\mathcal{S}}_o + \sum_{i=1}^{2} \boldsymbol{\mathcal{M}}_i \frac{d_{oi}}{\sigma_{fi}\delta} \log \left[1 + \delta \exp\left(\frac{d_i}{d_{oi}}\right) - \delta \right] \tag{72}$$

or, when the retention factor $\delta = 0$,

$$\boldsymbol{\mathcal{S}}(d) = \boldsymbol{\mathcal{S}}_o + \sum_{i=1}^{2} \boldsymbol{\mathcal{M}}_i \frac{d_{oi}}{\sigma_{fi}} \left(\exp\left(\frac{d_i}{d_{oi}}\right) - 1 \right). \tag{73}$$

Here $\boldsymbol{\mathcal{S}}_o$ denotes the initial material compliance. Equations (72) or (73) along with damage surface definitions and the Kuhn-Tucker conditions implied by (66)-(67) specify the complete (matrix) damage relationship. When $\delta = 0$, the damage-induced energy dissipation per unit initial volume is given by

$$\Omega_{di} = \frac{d_{oi}\,\sigma_{fi}}{2}. \tag{74}$$

Both the fiber and matrix materials are idealized with the constitutive model just developed; however, plasticity and the second damage mechanisms are omitted from the fiber model. All material quantities used in the respective models as well as the stress and strain vectors are those associated with the specific constituent.

2.3.2 Simplified Fiber-Direction Damage Model

A simplified strain-based fiber-direction failure criteria is now developed. This is done for numerical reasons, to eliminate the need to concurrently iterate on multiple damage and plasticity surfaces, as well as for practical and physical reasons. Presently, it is difficult to determine all the material coefficients needed for the fiber-direction tensile damage mechanism. Furthermore, experimental evidence suggests that fiber-direction strain is equally reliable in determining failure as is its associated stress-based criteria.

Consider uni-axial fiber-direction loading. Based upon (5), the composite stress is given by

$$\sigma^c_{11\,f} = v^f \sigma^f_{11\,f} + v^m \sigma^m_{11\,f} \tag{75}$$

or, under purely elastic conditions,

$$\sigma^c_{11\,f} = \left(v^f E^f_{11} + v^m E^m\right) \epsilon^c_{11}. \tag{76}$$

Since $v^f E^f_{11} \gg v^m E^m$ in composites consider here, it is reasonable to assume that at the onset of fiber-direction failure the matrix contribution to the overall composite stress is negligible, *i.e.*,

$$v^f \sigma^f_{11} \gg v^m \sigma^m_{11}, \tag{77}$$

and that failure initiation is controlled solely by the fiber contribution, *i.e.*,

$$\sigma^c_{11\,f} \approx v^f\, E^f_{11}\, \epsilon^c_{11}. \tag{78}$$

Note that non-linear matrix behavior typically initiates prior to composite failure so that $\sigma^m_{11} < E^m \epsilon^c_{11\,f}$.

The assumption that fiber-direction tensile failure is controlled by the fiber quantities is support by Swanson and co-workers (Swanson *et al*, 1987). They performed bi-axial testing on several carbon-fiber uni-directional composites, and concluded that $\epsilon^c_{11\,f}$ does not vary with physically achievable bi-axial loads - including shear. Observations made by DeTeresa (2000) indicate that shear failure in low-modulus carbon-fiber composites differs from that observed in high-modulus carbon-fiber composites. In high-modulus systems, the fiber fails in shear perpendicular to the fiber direction where as in low-modulus systems, the matrix fails parallel to the fiber direction. For low-modulus systems, this implies that shear does not induce a fiber-direction tensile failure mode. Thus, for low-

modulus carbon-fiber systems it is reasonable to define $\mathcal{M}_1$ as

$$\mathcal{M}_1 = \begin{bmatrix} < \sigma_{11} > & 0 & 0 & 0 & 0 \\ 0 & 0 & 0 & 0 & 0 \\ 0 & 0 & \text{“0”} & 0 & 0 \\ 0 & 0 & 0 & 0 & 0 \\ 0 & 0 & 0 & 0 & \text{“0”} \end{bmatrix}. \tag{79}$$

Use of (79) in ϕ^f_{d1} results in the classic stress-based fiber-direction failure criteria.

Several ways exist to transform the present stress-based criteria to a nearly equivalent strain based criteria. The two easiest methods, which yield equivalent results, are to assume that $\nu_{12} = \nu_{13} = 0$ or to consider a one-dimensional idealization. The former is now used along with (79).

Consider the damage surface ϕ_{d1} with $\mathcal{M}_1$ given by (79). With $\nu_{12} = 0$, S_{12}, S_{21}, C_{12}, and C_{21} are all zero. By use of (72) or (73) along with (48), the damage surface can be expressed as

$$\phi_{di} = \epsilon_{11}\left(E_{11}+ < \epsilon_{11} > \frac{d_{o1}}{\sigma_{f1}\delta}\log\left[1+\delta\left(X_1-1\right)\right]\right) - \sigma_{f1}\left(\frac{1-\delta}{X_1}+\delta\right) \tag{80}$$

or, when $\delta = 0$,

$$\phi_{di} = \epsilon_{11}\left(E_{11}+ < \epsilon_{11} > \frac{d_{o1}}{\sigma_{f1}}\left(X_1-1\right)\right) - \frac{\sigma_{f1}}{X_1}, \tag{81}$$

where

$$X_i = \exp\left(\frac{d_i}{d_{oi}}\right). \tag{82}$$

Noting that $\phi_{d1} = 0$ during active damage, the evolution of the internal damage variable X_1 can be explicitly given in terms of ϵ_{11} as

$$X_1 = \max\left[X_1, \frac{\left(1+\delta\left(X_1-1\right)\right)\left(\epsilon_{f1}+d_{01}\log\left[1+\delta\left(X_1-1\right)\right]\right)}{\delta\,\epsilon_{11} < \epsilon_{11} >}\right] \tag{83}$$

and when $\delta = 0$

$$X_1 = \max\left[X_1, \frac{\epsilon_{f1}-d_{01}}{< \epsilon_{11} > \epsilon_{11} - d_{01}}\right]. \tag{84}$$

Caution must be used when numerically employing either of these expressions since a pole exists in (83) at $\epsilon_{11} = 0$ and in (84) at $< \epsilon_{11} > \epsilon_{11} = d_{01}$, and the equations are not valid beyond those points.

The above strain-based criteria does not differ substantially from the previously proposed stress-based criteria. Zywicz (1999) showed that the differences in using the fiber-direction strain criteria instead of the fiber-direction stress criteria are relatively small for

elastic solids with a high degree of elastic orthotropy. For an AS4/3501-6 uni-directional composite with a longitudinal to transverse moduli ratio of 10, the maximum normalized difference was less than 7% for bi-axial transverse strains equal to or less than the longitudinal failure strain. Furthermore, Swanson's experimental results support the use of a fiber-direction strain criteria.

2.3.3 Utilization

Equation (78) suggests that any matrix damage which evolves before fiber damage initiates has little impact on the axial response. Similarly, matrix degradation that evolves after the fibers become fully damaged does not appear very important. Thus, it is convenient and practical to couple the fiber and matrix fiber-direction damage mechanisms together so that matrix and fiber damage initiates, evolves, and terminates simultaneously.

The fiber-direction damage mechanisms of the fiber and matrix are coupled together by using common values of d_1 and d_{o1}. With ϵ_{f1} interpreted as the composite's fiber-direction strain at the onset of failure, (84) is used to evolve the damage variable. The material constant d_{o1} is calculated as

$$d_{o1} = \frac{2\Omega_{d1}}{\sigma^c_{f1}}, \tag{85}$$

where Ω_{d1} is the fiber-direction damage energy of the composite and $\sigma^c_{f1} = E^c_{11}\epsilon^c_{1f}$. (The latter idealization ignores plasticity in the matrix contribution.)

The present damage model is regularized to generate mesh independent results using the approach developed by Oliver (1989) and Hillerborg (1976). The approach assumes that a single crack forms in an element for each damage mode. Oliver modifies the constitutive model constants such that the energy dissipated constitutively in the element, $(D_p+D_d)V$, equals the material's fracture energy, $\mathcal{G}$, times the element's postulated crack area A. The material constant d_o for each element is calculated as

$$d_o = 2\frac{\mathcal{G}/l - D_p}{\sigma^c_f}, \tag{86}$$

where $l = V/A$ and V is the element volume. Furthermore, to ensure a finite sound speed and a finite softening modulus,

$$d_o > 2\frac{\Omega^e}{\sigma^c_f}, \tag{87}$$

where Ω^e is the stored elastic energy density at failure. In the current implementation, (87) is satisfied in each element by increasing the element's value of $\mathcal{G}$ as necessary.

A simply modification can be introduce to model multiple crack formation per element. Let $1/\rho_c$ define the distance between cracks normal to the crack face. If the element length l is greater than $1/\rho_c$, then d_o is calculated as

$$d_o = 2\frac{\rho_c \mathcal{G} - D_p}{\sigma_f^c}. \tag{88}$$

The technique can only be applied in situations where ρ_c is know *a priori*.

2.4 Plane-Stress Plasticity

Matrix plasticity is modeled with a conventional J2 power-law relationship. The plane-stress yield surface is given by

$$\phi_p^2 = \boldsymbol{\sigma}^m : \boldsymbol{P} : \boldsymbol{\sigma}^m - G^2\left(\bar{\epsilon}^p\right), \tag{89}$$

where $\boldsymbol{P}$, the plane-stress projection operator (*e.g.*, see Simo and Taylor, 1986), is given by

$$\boldsymbol{P} = \begin{bmatrix} 1 & -1/2 & 0 & 0 & 0 \\ -1/2 & 1 & 0 & 0 & 0 \\ 0 & 0 & 3 & 0 & 0 \\ 0 & 0 & 0 & 3 & 0 \\ 0 & 0 & 0 & 0 & 3 \end{bmatrix}, \tag{90}$$

the hardening law by

$$G\left(\bar{\epsilon}^p\right) = k\left(\epsilon_0 + \bar{\epsilon}^p\right)^n, \tag{91}$$

and k, ϵ_0, and n are material constants. Plastic flow occurs normal to the flow surface such that

$$\dot{\epsilon} = \lambda \boldsymbol{P} : \boldsymbol{\sigma}^m \tag{92}$$

and

$$\dot{\bar{\epsilon}}^p = \lambda \sqrt{\boldsymbol{\sigma}^m : \boldsymbol{PEP} : \boldsymbol{\sigma}^m}, \tag{93}$$

where

$$\boldsymbol{E} = \begin{bmatrix} 4/3 & 2/3 & 0 & 0 & 0 \\ 2/3 & 4/3 & 0 & 0 & 0 \\ 0 & 0 & 1/3 & 0 & 0 \\ 0 & 0 & 0 & 1/3 & 0 \\ 0 & 0 & 0 & 0 & 1/3 \end{bmatrix} \tag{94}$$

E_t (GPa)	E_l (GPa)	μ_{lt} (GPa)	ν_{lt}	ν_{tt}
234.3	34.5	24.1	0.30	0.40

Table 1: Carbon fiber properties

and λ is the consistency parameter. To satisfy the inherent Kuhn-Tucker constraint,

$$\phi_p \lambda = 0, \quad \phi_p \leq 0, \quad \text{and} \quad \lambda \geq 0. \tag{95}$$

2.5 Validation

The homogenized tow-level constitutive model was implemented in DYNA3D (Whirley and Englemann, 1993) and compared to detailed 3-D micromechanical FE simulations. The micromechanical model idealized the fiber packing as hexagonal in the tow and modeled the individual fiber and matrix discretely as shown in Figure 1. The fiber was considered to be a transversely isotropic elastic solid with the elastic constants given in Table 1. The matrix was taken as an isotropic elasto-plastic solid with a Young's modulus of 4.35 GPa, a Poisson's ratio of 0.36, and a power-law flow stress given by $117.1\,(\bar{\epsilon}^p + 5 \times 10^{-4})^{0.04}$ MPa. Table 2 summaries the effective elastic constants of the tow for various fiber volume fractions. Overall, the tow model predictions agree reasonably well with the hexagonal idealization for all fiber volume fractions considered.

The consistent μ_{lt} value from the homogenization is less than half the hexagonal packing value. Because the homogenized tow behavior is transversely-isotropic and σ_{lt} depends solely on γ_{lt}, alternative homogenization schemes can be used to calculate μ_{lt} without altering the other coefficients or, in general, the basic homogenization assumptions. For the present material, the value of μ_{lt} calculated from the composite cylinder model (Hasin, 1983) is much larger than the hexagonal packing values. However the average of the two homogenization schemes yields a μ_{lt} value very close to the hexagonal-based value. Thus, the averaged μ_{lt}, denoted as μ_{lt}^*, is used in the present model.

Various elasto-plastic comparisons were performed between the tow model and the hexagonal FE model. These calculations assumed $v^f = 0.70$ and imposed peak macroscopic strain levels of 0.02. Under uni-axial longitudinal loading, both responses appear nearly linear during loading and unloading, and differ in proportion to their longitudinal Young's moduli. The hexagonal model does develop a small plastic axial strain of 0.06% by the end of the loading cycle. Similar behavior was observed for the other bi-axial and tri-axial loadings examined. These include: 1) bi-axial loading in the transverse

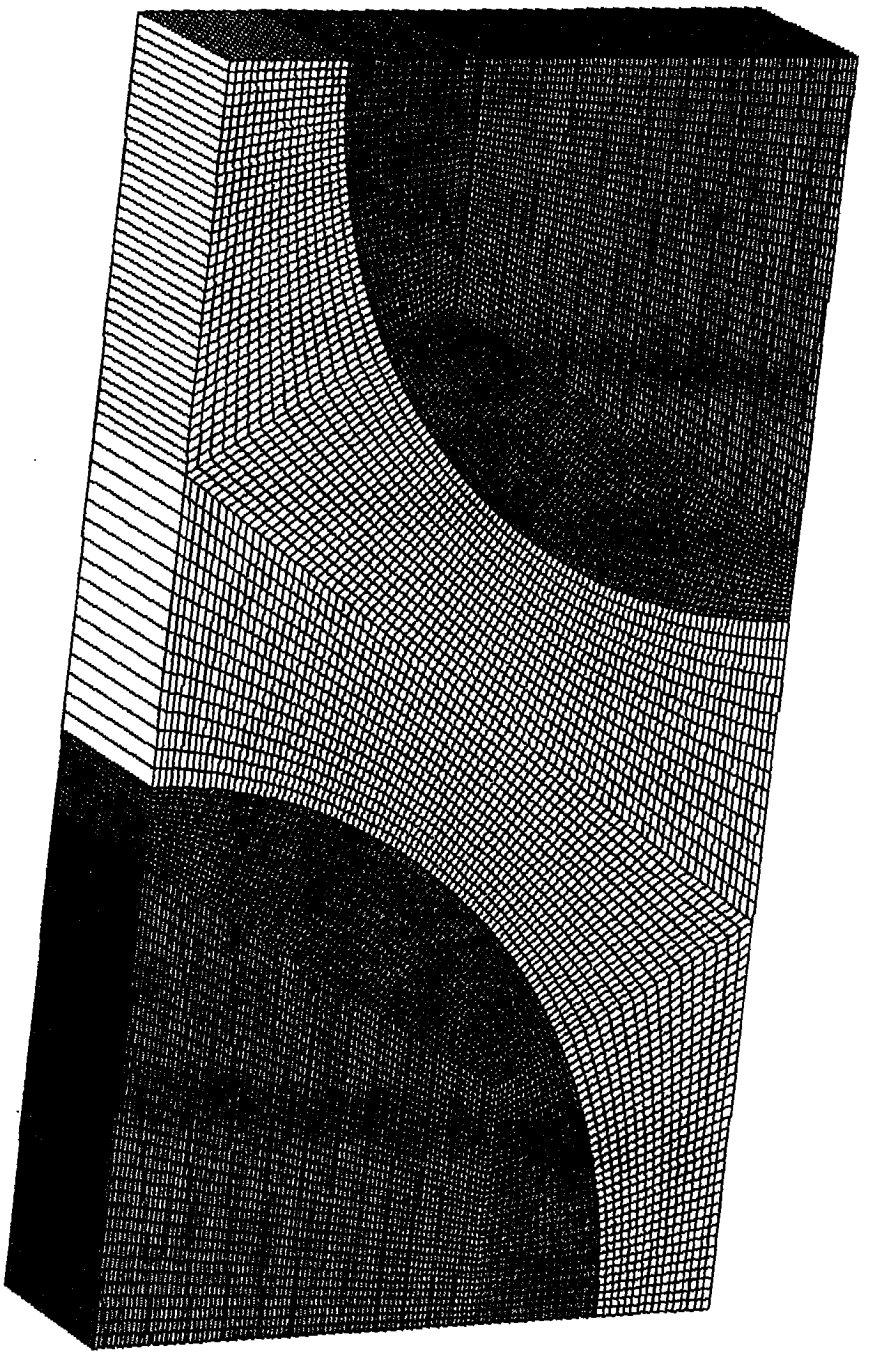

Figure 1: Mesh of hexagonal tow RVE

v^f	Model	E_l (GPa)	E_t (GPa)	μ_{tt} (GPa)	μ_{lt} (GPa)	ν_{tt}	ν_{lt}
0.5	FE	111.0	7.558	2.170	2.770	0.480	0.326
	Tow	118.6	6.428	2.088	2.610	0.540	0.330
0.6	FE	134.0	9.267	3.183	3.445	0.455	0.323
	Tow	141.8	7.682	2.501	3.272	0.535	0.324
0.7	FE	155.8	11.65	4.072	4.403	0.430	0.317
	Tow	164.9	9.536	3.121	4.279	0.526	0.318
0.8	FE	177.5	15.09	5.347	5.914	0.411	0.312
	Tow	188.0	12.56	4.161	6.316	0.511	0.312

Table 2: Predict effective tow properties from FE calculations and the tow constitutive model

direction with ratios of 2:2 and 2:1, and 2) tri-axial loading with an axial to transverse to transverse strain ratio of 2:2:1. The largest differences between the tow and hexagonal model occurred in uni-axial transverse loading. Figure 2 shows the stress-strain curves. Figure 3 shows the longitudinal-transverse shear-stress versus shear-strain response for v^f equal to 0.5, 0.6, 0.7, and 0.8 calculated by the tow model and from micromechanical simulations based upon hexagonal fiber packing. The figure includes a FE simulated response for a square fiber array with $v^f = 0.70$. Little difference exists between the tow model and hexagonal idealization for all v^f examined. While the square, hexagonal, and tow results for $v^f = 0.7$ are similar at larger strains, the square idealization differences substantially from the other results for small strains.

Engineering judgment must be exercised when comparing results from different models. The hexagonal packing idealization used here represents one of many possible fiber arrangements. Unfortunately, each idealization yields slightly different elastic coefficients and macroscopic behavior. For example, similar FE simulations for a square packing array with $v^f = 0.70$ predict that μ_{lt} is 5.93 GPa - 35% larger than the present hexagonal idealization. On the other hand, Hasin and Rosen's (1964) composite cylinder assemblage model yields a longitudinal modulus that is always larger than the present tow model which in turn is larger than the hexagonal model (for the current material). While certain models are easier to work with, no geometrical idealization captures the actual fiber distribution in the composite and consequently the composite's exact response.

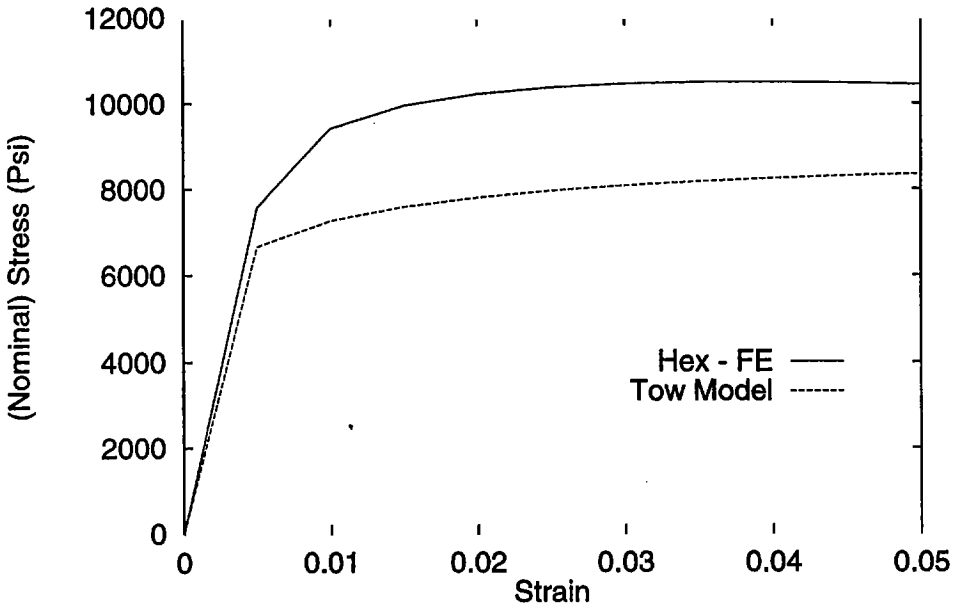

Figure 2: Uni-axial stress response in the transverse direction

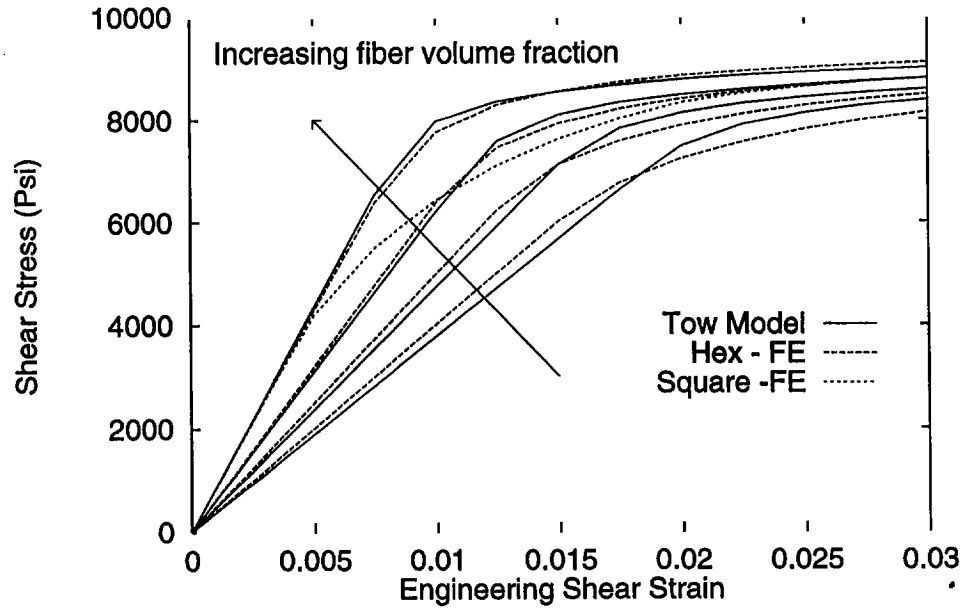

Figure 3: Longitudinal shear stress response - $v^f = 0.5$, 0.6, 0.7, and 0.8

3 Simplified Representative Volume Element

The braid RVE is shown schematically in Figure 4 and is the same idealization used in Zywicz and Nguyen (1999) and Zywicz *et al* (2000). The RVE contains two flat 0° axial tows, two pairs of piecewise linear undulating braider tows oriented in the $+\theta$ and $-\theta$ direction, and several resin pockets. The tows are braided in a 2×2 pattern and have rectangular cross sections t thick and d wide. (Subscripts a and b denote the individual axial and braider tow quantities, respectively.) The $\pm\theta$ braider crossover junction is offset from the braider-axial tow crossover junction. The RVE is $2w$ wide and t thick, where w is the inter-axial tow spacing, and t is given by

$$t = t_a + 2t_b. \tag{96}$$

Each tow contains m_f filaments with an average filament diameter of d_f. (Note, m_f and d_f need not be the same in the axial tow and braider tows.) Consequently, p, the tow packing density (or tow fiber volume fraction) is expressed as

$$p = \frac{m_f \, d_f^2 \, \pi/4}{d \, t}. \tag{97}$$

When t is small compared to w and l, the overall RVE fiber volume fraction is approximately

$$V_f \approx \frac{\pi}{4wt} \left(m_{f\,a} \, d_{f\,a}^2 + \sqrt{1 + \tan^2\theta} \, m_{f\,b} \, d_{f\,b}^2 \right). \tag{98}$$

The braider tows parallel the RVE mid-surface except in the undulation region where they are inclined from the mid-surface by ϕ, the crimp angle. The crimp angle depends strongly upon the d_b and the two thicknesses, and is given by

$$\phi = \tan^{-1} \frac{(t_a + t_b)\cos(\pi/2 - 2\theta)}{w\cos\theta - d_b} \tag{99}$$

In the RVE plane, the undulation regions appear as parallelograms whose vertices lie on the edges of the axial tows and opposite fiber direction braider tows. Thus, in order for the braiders to undulate, $d_a \leq w/2$ and $d_b \leq w\cos\theta$.

The RVE contains some rather artificial microstructural features. Undulations and in-plane curvature in the axial tows are absent while the braider tows are represented as piecewise linear sections. This creates appreciable pure resin "pockets" around the undulations, yields an overly large ϕ for higher V_f, and produces a discontinuous fiber direction in the braiders. Consequently, neither tow representation depicts the true

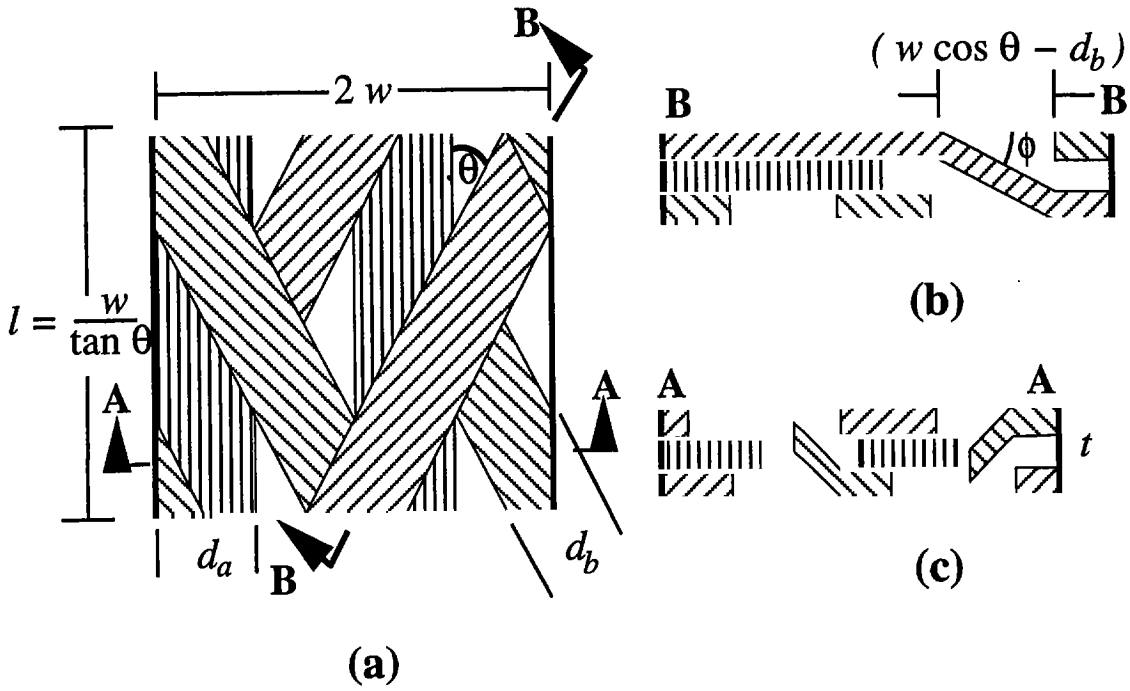

Figure 4: RVE **a**) top view, **b**) section parallel to braider tow, and **c**) section perpendicular to axial tow

θ	t (mm)	t_b (mm)	d_b (mm)	l (mm)	ϕ
30^o	1.550	0.467	6.647	17.60	23.5^o
45^o	1.753	0.569	5.462	10.16	34.5^o
60^o	2.286	0.836	3.721	5.866	42.7^o

Table 3: RVE dimensions and crimp angle

meandering geometry of the fibers or the dense melded appearance present in sectional micrographs. (Note, the natural tendency for the upper and lower braider tows to curve toward the mid-surface near the undulation pockets reduces the pocket size and ϕ in the actual composite material.)

Table 3 summarizes the RVE dimensions for three large-tow carbon-fiber tri-axial braids. In each, the axial and braider tows contain 80,000 filaments with an average d_f of 6.2 μm, V_f is approximately 50%, p_a and p_b are 75%, and w is 10.16 mm. To minimize ϕ, d_a is set equal to $w/2$. Thus from (97), t_a is 0.613 mm.

4 3-Layer Numerical Braid Model

The 3-layer numerical braid model is now presented. First, the simplified braid RVE geometry and idealizations are explained. Next, an explicit undulation model is assembled. Lastly, the integration rules to use this model with traditional shell elements in FE simulations are summarized.

4.1 3-Layer Braid RVE

The braid RVE is further simplified to allow numerical modeling. The RVE is sectioned into three layers as shown in Figure 5. The axial tows reside completely within the middle layer while the flat portions of the $\pm\theta$ braiders populate the upper and lower layers. In the middle layer, the fibers in the undulations are neglected so that it consists conceptually of pure resin and axial tow regions. The layer is "homogenized" by assuming an iso-strain state in the fiber direction and iso-stress state in all other directions. The homogenization yields the previous tow-level model except the effective fiber volume fraction is now given by

$$v_a^f = \frac{m_{fa} d_{fa}^2 \pi/4}{t_a w}. \tag{100}$$

In the upper and lower layers, the braider fibers, including half the projected undulation portions that reside in the middle layer, are segregated within each layer with their surrounding resin regions. A similar homogenization is applied in each region which effectively just reduces the braider v^f so that the effective braider fiber volume fraction becomes

$$v_b^f = \frac{m_{fb} d_{fb}^2 \pi / 4}{t_b \, w \cos\theta}. \tag{101}$$

Several additional idealizations are made regarding the upper and lower layers. It is assumed that there are two coincidental upper and lower layers, and that the effective braider material for each direction occupies one entire upper and lower layer. To obtain the correct net RVE surface tractions, only half the effective braider stress are included in the overall braid response. The distance the extreme layers are offset from the neutral surface can differ in the numerical and physical RVE models. Finally, the influence of undulations is limited and does not couple the behavior of the respective upper and lower braider tows.

4.2 Undulations

The effects of braider undulations are included via a 1-dimensional undulation model that is selectively added, in series, to the tow model. The fiber-direction strain is split into a undulation portion, ϵ^u, and a straight portion, ϵ_{11}^s, as

$$\epsilon_{11} = \lambda \epsilon^u + (1 - \lambda)\, \epsilon_{11}^s, \tag{102}$$

where λ is the undulation length fraction. For the present braid RVE, λ is expressed as

$$\lambda = \frac{\cos\theta - d_b/w}{\cos\left(\pi/2 - 2\theta\right)\, \sqrt{1 + 1/\tan^2\theta}}. \tag{103}$$

The undulation stress, σ^u, is functionally given by

$$\sigma^u = C^u \left(\epsilon^u - \epsilon^{u\,p}\right), \tag{104}$$

where $\epsilon^{u\,p}$ is the plastic undulation strain and C^u is the undulation modulus. Detailed numerical simulations of the undulation region show that the tensile response smoothly transitions from an initial linear response to a softer secondary linear region. (See Figure 6.) In compression, the response is nearly elastic/perfectly-plastic. However, both

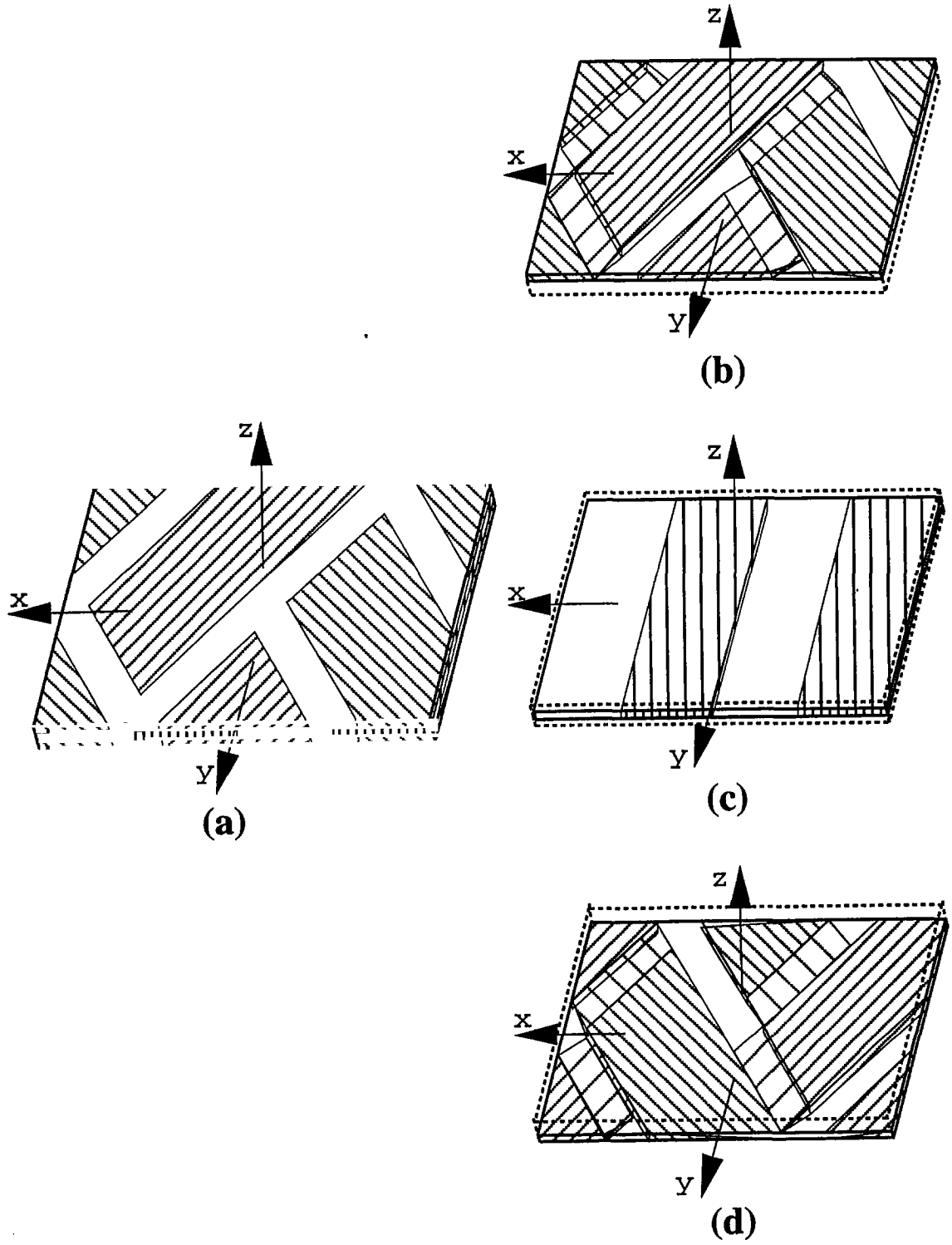

Figure 5: 3-layer idealization **a**) RVE, **b**) top layer, **c**) middle layer, and **d**) bottom layer

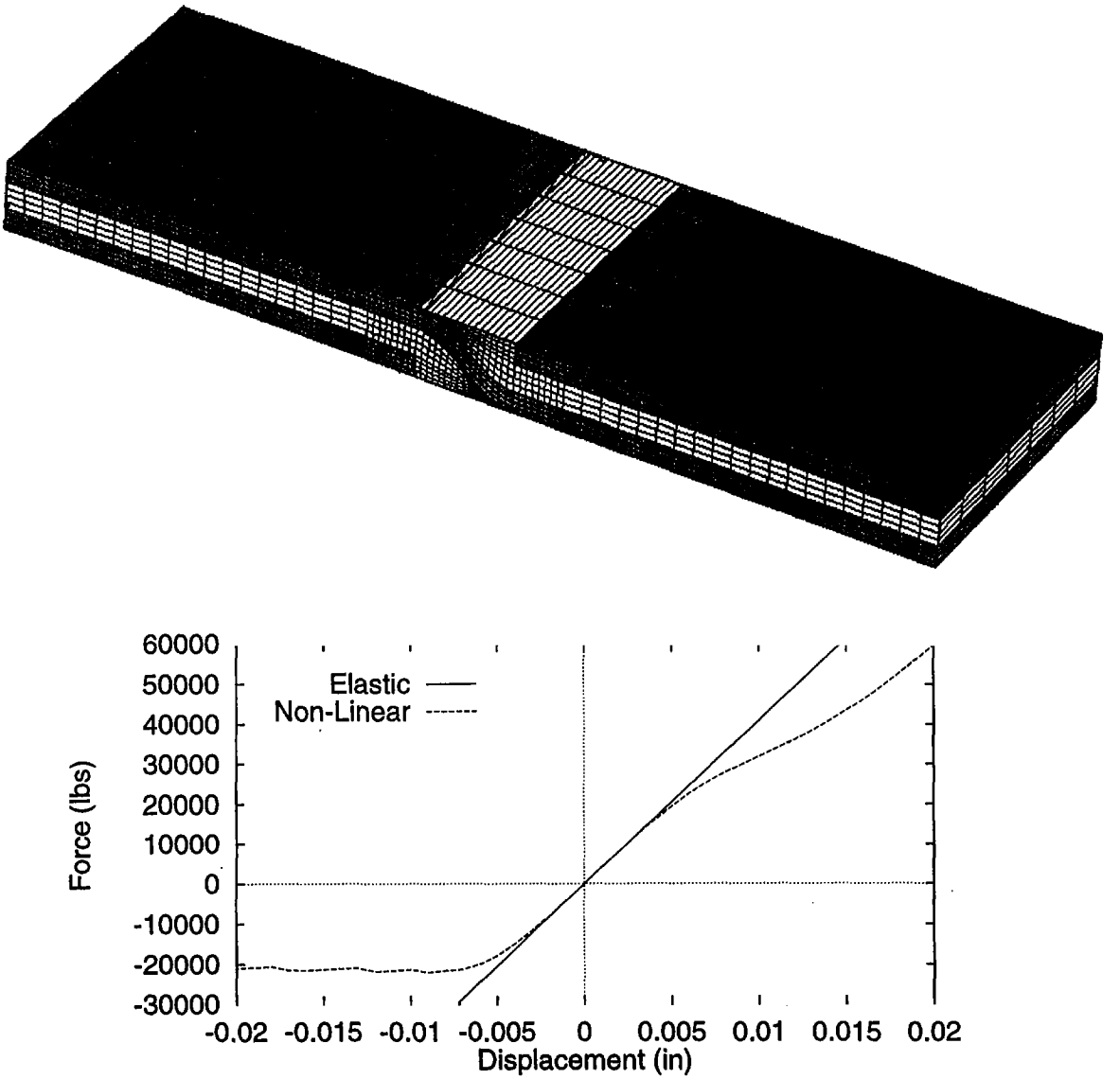

Figure 6: FE undulation model and its predicted force-displacement behavior

the tensile and compressive behavior depend strongly on the adjacent material and constraints. At present, C^u is taken as constant Until a more accurate relationship is assembled, $\epsilon^{u\,p}$ is neglected and C^u is taken as constant.

Naik (1995) developed an undulation model from solutions for an elastic curved beam on an elastic foundation. C^u is obtained by linearizing his model about zero axial load and averaging the strain in the undulation region. This yields

$$S^u = \frac{1}{C^u} = \frac{B\left(1-B\right)^3}{8\left(E_{11}^c B^3\left(1-B\right)/12 + 8\left(L_u/t\right)^4 Z E^m/\pi^4\right)} + \frac{1}{E_{11}^c}, \tag{105}$$

where

$$\dot{Z} = a\left(\frac{a}{\sqrt{a^2-1}-1}\right), \tag{106}$$

$$a = 3 + \frac{2B}{1-B}, \tag{107}$$

$$A = t_a/t, \qquad B = t_b/t, \qquad \text{and} \qquad L_u = \lambda w\sqrt{1+1/\tan^2\theta}. \tag{108}$$

Here E_{11}^c is the Young's modulus of the braider tow obtained using the original RVE packing fraction, p_b. Unlike the original formulation, the matrix modulus is used for the elastic foundation stiffness. (This yields better agreement with detailed FE simulations of the braid RVE.)

4.3 Numerical Utilization

The present braid model is designed to be used in traditional shell elements with a modified through-thickness integration rule. To accurately capture the elastic flexural response, 10 through-thickness integration points must be used and be positioned at specified locations. The integration weights, ω, and locations, ζ $(-1 \leq \zeta \leq 1)$, are summarized in Table 4. In select applications, 5 through-thickness integration points can be used. The conventional integration weights and locations are listed in Table 5, however, alternative braider locations might provide better integration of the flexural response.

5 3-Layer Braid Model Validation

The elasto-plastic response of the 3-layer braid model was compared to detailed, 3-D FE simulations of the braid RVE. Three braid angles were examined: $\theta = 30^o$, 45^o, and

Tow	Point	ω	ζ
Axial	1	A	$A/\sqrt{3}$
Axial	2	A	$-A/\sqrt{3}$
$+\theta$ Braider	3	$B/2$	$A+B(1+1/\sqrt{3})$
$-\theta$ Braider	4	$B/2$	$A+B(1+1/\sqrt{3})$
$+\theta$ Braider	5	$B/2$	$A+B(1-1/\sqrt{3})$
$-\theta$ Braider	6	$B/2$	$A+B(1-1/\sqrt{3})$
$+\theta$ Braider	7	$B/2$	$-A-B(1+1/\sqrt{3})$
$-\theta$ Braider	8	$B/2$	$-A-B(1+1/\sqrt{3})$
$+\theta$ Braider	9	$B/2$	$-A-B(1-1/\sqrt{3})$
$-\theta$ Braider	10	$B/2$	$-A-B(1-1/\sqrt{3})$

Table 4: Weights and positions for 10 point integration

Tow	Point	ω	ζ
Axial	1	$2A$	0
$+\theta$ Braider	2	B	$A+B/2$
$-\theta$ Braider	3	B	$A+B/2$
$-\theta$ Braider	4	B	$-A-B/2$
$+\theta$ Braider	5	B	$-A-B/2$

Table 5: Weights and positions for 5 point integration

θ	Model	Extension				Flexure		
		E_l	E_t	ν_{lt}	μ_{lt}	E_l	E_t	ν_{lt}
30^o	3-Layer	56.1	8.08	1.15	12.0	35.0	7.61	1.35
	FE	59.8	8.82	1.07	11.0	32.5	8.37	0.946
45^o	3-Layer	38.8	15.1	0.726	14.3	14.2	12.5	0.764
	FE	40.1	15.1	0.686	11.5	15.0	12.5	0.631
60^o	3-Layer	29.3	33.6	0.322	12.8	8.61	31.0	0.322
	FE	29.8	25.9	0.300	8.48	9.00	23.5	0.283

Table 6: Predicted and simulated braid properties (units - GPa)

60^o. The continuum FE model, described in Zywicz and Nguyen (1999) and Zywicz *et al* (2000), used the fiber and matrix properties summarized in Table 1 and section 2.5. Periodic boundary conditions were imposed on the RVE to infer the effective elastic properties. Table 6 summaries the elastic properties of the braid RVE obtained from the 3-layer model and the detailed FE simulations. In the 3-layer model, the undulation stiffness has a strong influence on the braider dominated properties E_t, ν_{lt}, and μ_{lt}, especially for the larger braid angles. For example, a 30% reduction in C^u lowered the extensional E_t and μ_{lt} properties for $\theta = 60^o$ slightly below the FE based values, but left E_l unchanged.

The elasto-plastic response of the 3-layer model and the detailed continuum RVE model are plotted in Figures 7-11 for uni-axial extension, simple shear, and uni-axial flexure. In all cases, the differences in the initial elastic responses reflect the differences in elastic moduli summarized in Table 6. As evident from Figure 7, good agreement exits between both model predictions for uni-axial longitudinal extension for all braider angles. In uni-axial transverse extension and longitudinal-transverse shear, Figures 8 and 9, agreement between the two models deteriorates at higher strain levels as the braider angle increases and the axial response of the braiders become more significant. Examination of the 3-layer model shows that under longitudinal-transverse shear, the axial behavior of the braider tows dominate the overall response, while in transverse extension, this occurs only when θ is large.

The strains in the braider tows at maximum imposed shear strain were quantified using the 3-layer model. Based upon the previous FE undulation modeling, the stress at the corresponding axial strain was estimated. For the braider tow in compression, the corresponding axial stress was less than one-third, in magnitude, than that predicted by

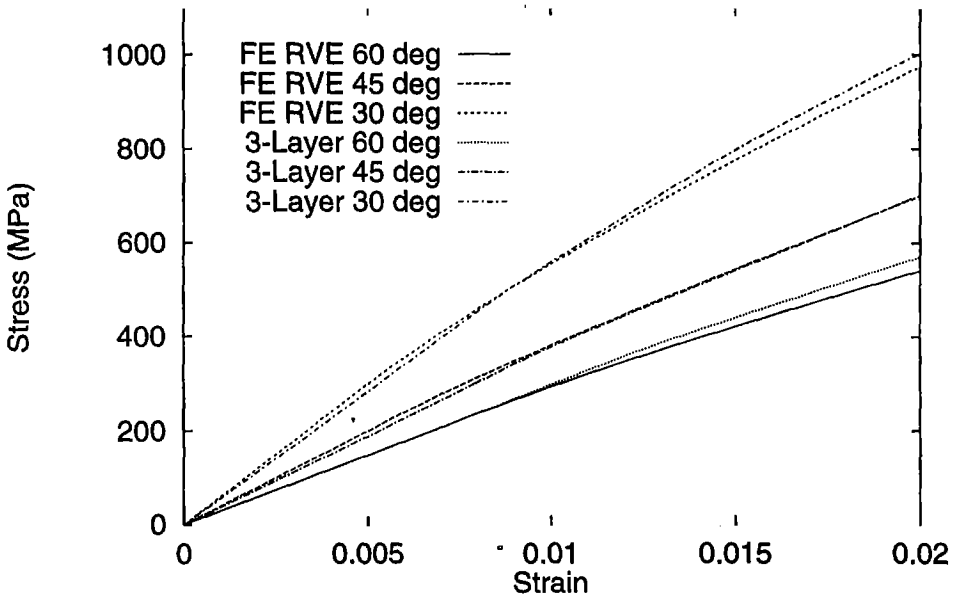

Figure 7: Longitudinal uni-axial stress-strain response

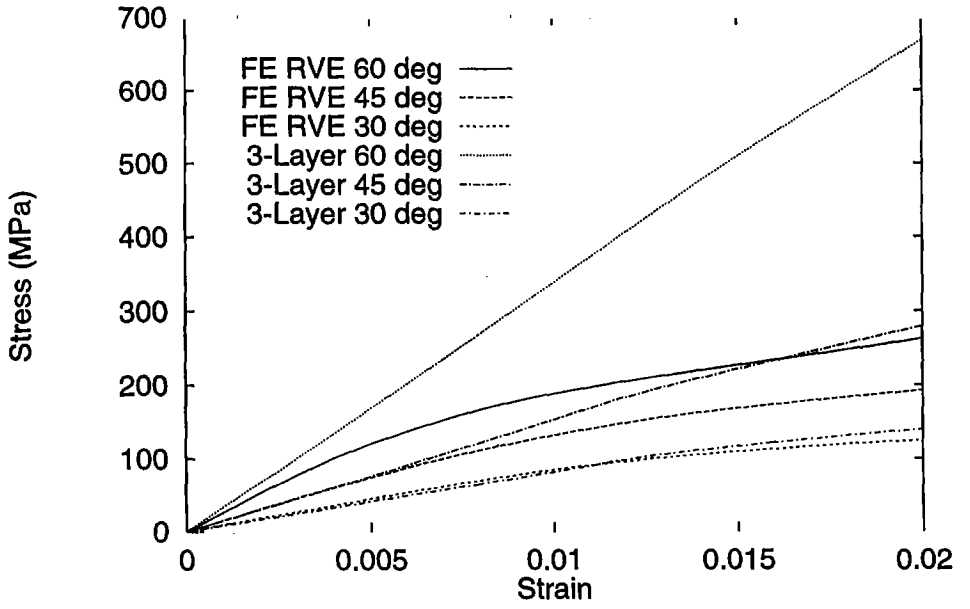

Figure 8: Transverse uni-axial stress-strain response

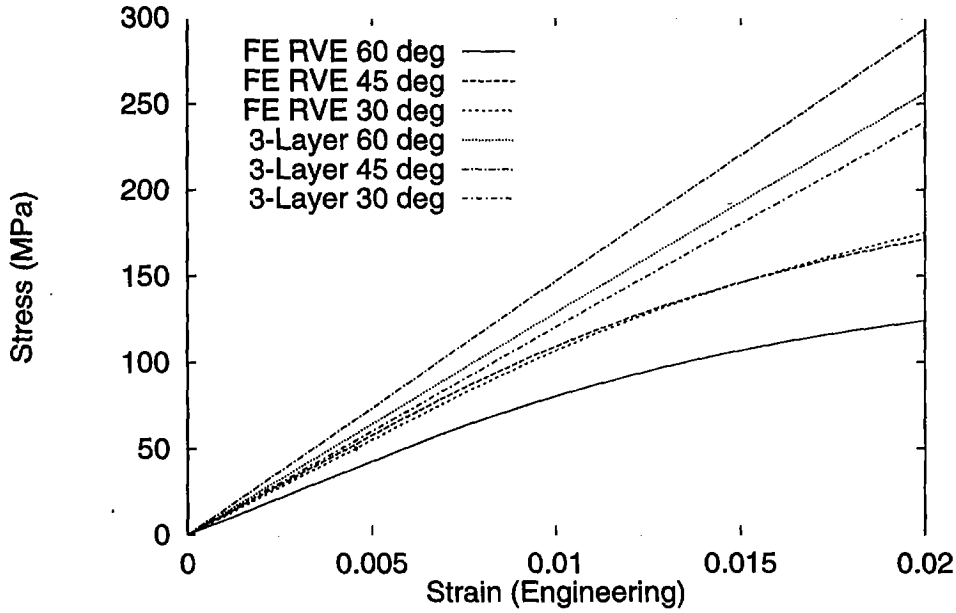

Figure 9: Longitudinal-transverse shear stress-strain response

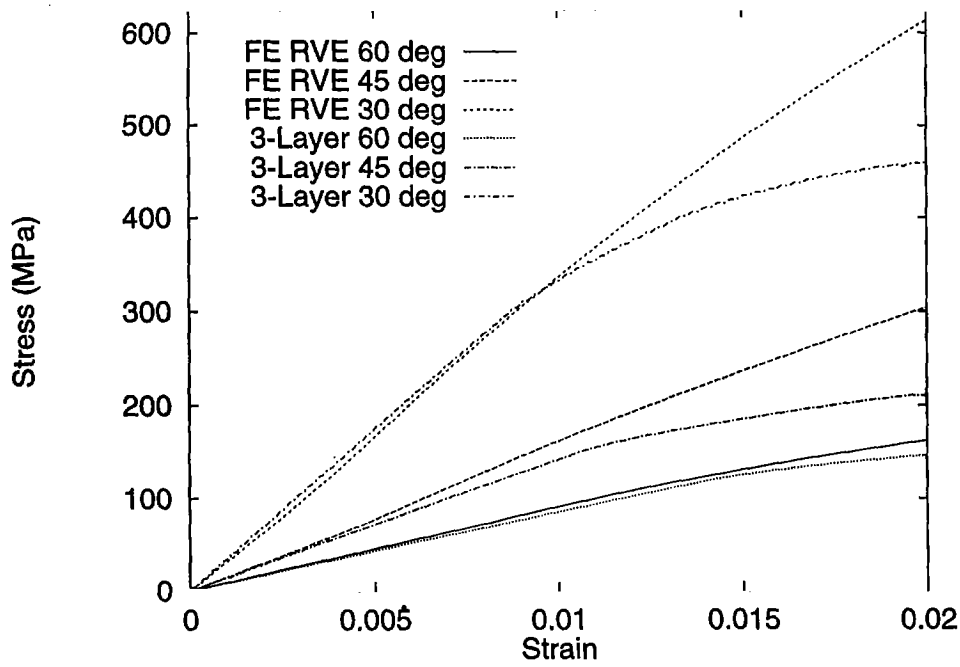

Figure 10: Longitudinal flexure - pseudo stress-strain response of upper surface

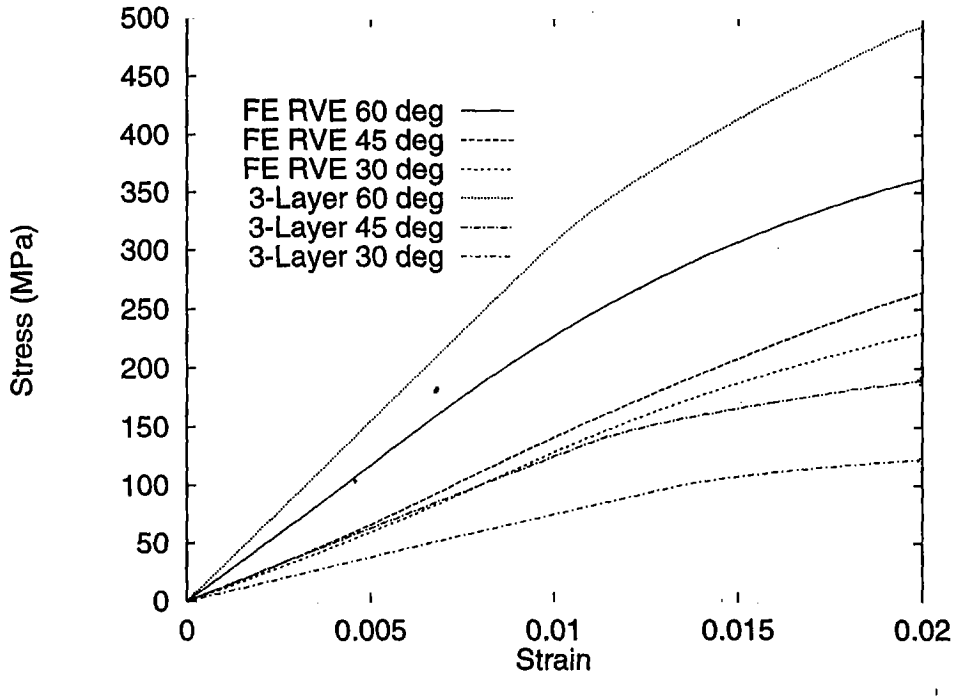

Figure 11: Transverse flexure - pseudo stress-strain response of upper surface

the 3-layer model. The inclusion of an appropriate undulation model would therefore lower the shear response to a level much closer to that predicted by the FE RVE model.

The uni-axial flexural response was examined in the two primary directions. The moment-rotation curves have been transformed into pseudo macro stress-strain curves for a material point on the tensile surface and are plotted in Figures 10 and 11. The pseudo stress is calculated by assuming the distribution of macro stress is linear in the through-thickness direction, *i.e.*, an elastic idealization. Again, the difference in elastic moduli has a predictable influence on the initial portions of the curves. In all cases, the 3-layer longitudinal response predicts excessive strain softening compared to the RVE results, and the extra strain softening is not related to quadrature error. (Higher order integration yielded nearly identical results.) The source of this behavior is not presently understood.

Various simulations were performed to test the damage portion of the braid model with and without plasticity. The 3-layer model responded numerically as expected. With out a consistent set of material properties, the predictions are of limited use, and therefore not shown here. Nonetheless, validating the damage portion of the model against physical experiments possess the biggest challenge and remains to be accomplished.

6 Conclusion

A numerical approach to model the elasto-plastic and tensile damage response of tri-axially braided carbon-fiber polymeric-matrix composites has been developed. It consists of a simplified RVE geometry, a plane-stress tow-level constitutive relationship, a one-dimensional undulation relationship, and a non-traditional shell element integration rule. The tow-level constitutive model is micromechanically based and constructed from the fiber and matrix behavior. Its pre-damage response compares favorably with detailed FE micromechanical simulations of periodically arranged uni-directional composites. Tensile damage is included in the tow model to replicate, in a smeared manner, the evolution of cracks parallel and perpendicular to the fiber-direction. The influence of the undulation is captured by coupling the fiber-direction response with a one-dimensional undulation relationship at the tow level. The total braid response is achieved by integrating the 3-layer model in the through-thickness direction with a non-traditional shell element integration rule. The present tow-level model can also be used separately to model uni-directional lamina.

The braid model has been implemented in DYNA3D, and is fully compatible with traditional shell element formulations. The predicted elastic extensional, shear, and flexural braid properties agree reasonably well with more detailed micromechanical models for a broad range of braider angles. Comparisons of the inelastic braid behavior demonstrate similar good agreement when the axial tows dominate the response, but show larger discrepancies when the response is controlled by the braider tows. Under extensional and shear loadings, this deficiency arises from the lack of an appropriate non-linear undulation model.

While the present braid formulation includes elasticity, plasticity, and tensile damage, it lacks comprehensive compressive failure mechanisms and an adequate non-linear undulation model. The inclusions of the later features will yield a comprehensive formulation that can be applied to model a wide range of carbon-fiber textile composites. This includes the present tri-axially braided architectures as well as, with slight modification, woven, cloth, and even uni-directional fiber architectures.

Acknowledgments

This work was performed under the auspices of the U.S. D.O.E. by Lawrence Livermore National Laboratory under contract W-7405-Eng-48 and was supported by the

U.S. D.O.E., Office of Transportation Technologies, Lightweight Material Program under Dr. J. Carpenter and Mr. D. Warren. The author appreciates his interactions with the Automotive Composite Consortium.

7 References

Bažant, Z. P., and Planas, J., 1998, Fracture and Size Effect in Concrete and Other Quasibrittle Materials, CRC Press, Boca Raton.

Carrier, C. R., and Averill, R. C., 2000, "A Simple Discrete-Tow Model for Analysis of Textile Composites," Journal of Composites Technology and Research, **22**.

DeTeresa, S. J., 2000, Private communications.

Govindjee, S., Kay, G. J., and Simo, J. C., 1995, "Anisotropic Modelling and Numerical Simulation of Brittle Damage in Concrete," *International Journal for Numerical Methods in Engineering*, **38**, 3611-3633.

Hansen, N. R., and Schreyer, H. L., 1994, "A Thermodynamically Consistent Framework for Theories of Elastoplasticity Coupled with Damage," *International Journal of Solids and Structures*, **31**, 359-389.

Hashin, Z., and Rosen, B. W., 1964, "The Elastic Moduli of Fiber-Reinforced Materials," *ASME Journal of Applied Mechanics*, **31**, 223-232.

Hashin, Z., 1983, "Analysis of Composite Materials", *ASME Journal of Applied Mechanics*, **50**, 481-505.

Hillerborg, A. *et. al*, 1976, *Cement and Concrete Research*, **6**, 773-782.

Jones, R. M., 1975, Mechanics of Composite Materials, McGraw-Hill, New York.

Malvern, L. E., 1969, Introduction to the Mechanics of a Continuous Medium, Prentice-Hall, Inc., New Jersey, 223.

Naik, R. A., 1995, "Failure Analysis of Woven and Braided Fabric Reinforced Composites," *Journal of Composite Material*, **29**, 2334-2363.

Oliver, J., 1989, "A Consistent Characteristic Length for Smeared Cracking Models," *International Journal for Numerical Methods in Engineering*, **28**, 461-474.

Simo, J. C., (1989), "Strain Softening and Dissipation: A Unification of Approaches," Cracking and Damage: Strain Localization and Size Effects, eds. Mazars, J., and Bažant, Z. P., New York, Elsevier Applied Science, pp. 440-461.

Simo, J. C., and Taylor, R. L., 1986, "A Return Mapping Algorithm for Plane Stress Elastoplasticity," *International Journal for Numerical Methods in Engineering*, **22**, 649-670.

Puso, M. A., and Weiss, J. A., 1997, "Finite Element Implementation of Anisotropic Quasilinear Visocelasticity," *ASME Journal of Biomechanical Engineering*, **120**, 62-70.

Swanson, S. R., Messick, M. J., and Tian, Z., 1987, "Failure of Carbon/Epoxy Lamina Under Combined Stress," *Journal of Composite Materials*, **21**, 619-630.

Whirley, R. G., and Engelmann, B. E., 1993, "DYNA3D User Manual," University of California, UCRL-MA-107254, Rev. 1.

Whitcomb, J. D., Chapman, C. D., 1998, "Analysis of Plain Weave Composites Subjected to Flexure," *Mechanics of Composite Materials and Structures*, **5**, 41-53.

Zywicz, E., 1997, "DYNA3D Material Model 50: A Progress Composite Damage Model", University of California, LLNL, UCRL-ID-128518.

Zywicz, E., 1999, "On the Equivalence of Stress- and Strain-Based Failure Criteria in Elastic Media," *European Journal of Mechanics A-Solids*, **18**, 391-398.